Ecological Questions 37(2026)4 http://dx.doi.org/10.12775/EQ.2026.045

Shifts in Central Asia's Surface Energy Balance from 1948 to 2048: Historical Trends and Statistical Projections

Seyed Omid Reza Shobairi[1,*], Yaning Chen[1,2,*], Farhod Nasrulloev[1,3], Hossein Azadi[4], Behnam Asghari Beirami[5]

[1]Xinjiang Institute of Ecology and Geography, Chinese Academy of Sciences, Urumqi, 830011, China

[2]Xinjiang Laboratory of Lake Environment and Resources in Arid Zone, College of Geographic Science and Tourism, Xinjiang Normal University, Urumqi, 830054, China

[3]Institute of Water Problems, Hydropower and Ecology of the National Academy of Sciences of Tajikistan, Dushanbe 734042, Tajikistan

[4]Department of Geography, Ghent University, 9000 Ghent, Belgium

[5]K. N. Toosi University of Technology, Tehran, Iran

*Corresponding Author e-mail: omidshobeyri214@gmail.com

Received: 22 June 2025 / Accepted: 8 September 2026

Abstract. Central Asia, a critical climate hotspot with arid and semi-arid landscapes, has experienced significant hydroclimatic changes under global warming. This study examines spatiotemporal dynamics and future projections of sensible (SHF), latent (LHF), and ground (GHF) heat fluxes across the region from 1948 to 2048, using observational data (NASA Giovanni, 1948–2024) and statistical forecasts (2025–2048). Trend analyses reveal a significant decline in SHF (-0.082 W m^{-2} yr^{-1}, $p < 0.001$) and an increase in LHF (0.056 W m^{-2} yr^{-1}, $p < 0.001$), indicating a repartitioning of surface energy toward enhanced evapotranspiration driven by warming and wetting trends. GHF showed no significant change. Projections suggest continued SHF reductions and LHF increases, with uncertainties reflecting potential climate feedbacks. These findings have implications for drought risk, boundary-layer dynamics, and cryospheric changes in this geopolitically and ecologically sensitive region, and provide a reproducible framework for integrating heat flux trajectories into climate assessments.

Keywords: Surface Heat Fluxes, Central Asia, Climate Change, Land–Atmosphere Interactions, Evapotranspiration.

1. Introduction

Central Asia (CA), comprising Kazakhstan, Kyrgyzstan, Tajikistan, Turkmenistan, and Uzbekistan (Starr, 2011), spans approximately 4 million km² of diverse topography, from vast deserts like the

Karakum and Kyzylkum to high-altitude mountain ranges such as the Tien Shan and Pamir (Hu et al., 2014). This continental climate regime, marked by extreme temperature variability, low annual precipitation (typically 200–500 mm), and pronounced seasonality, renders the region highly susceptible to climate perturbations (Wang et al., 2023; Shobairi et al., 2024). Over the past century, CA has witnessed accelerated warming rates exceeding global averages, coupled with heterogeneous precipitation shifts, leading to recurrent droughts, glacial retreat, and altered hydrological cycles (Huang et al., 2021; Sadyrov et al., 2025). These changes profoundly impact the surface energy balance, wherein net radiation is partitioned into SHF (turbulent heat transfer to the atmosphere), LHF (energy expended in evapotranspiration), and GHF (conductive heat flow into the subsurface). Such partitioning governs near-surface meteorology, including temperature extremes, atmospheric stability, soil moisture regimes, and ecosystem productivity (Arya, 2001; Bonan, 2019). Despite extensive research on temperature and precipitation trends in CA, systematic analyses of surface heat fluxes over extended temporal scales remain sparse. Existing studies often focus on adjacent regions like the Tibetan Plateau (TP), where SHF variations influence monsoon dynamics (Yang et al., 2014; Chen et al., 2019), or global monsoon domains exhibiting shifts in LHF and SHF under climate change (Zeng & Zhang, 2020). In CA specifically, limited investigations highlight the role of soil moisture in modulating heatwaves and heat fluxes (Li et al., 2012; Wang et al., 2023), yet a comprehensive century-scale assessment integrating historical observations with robust projections is lacking. This gap hinders understanding of land–atmosphere feedbacks, particularly in arid environments where moisture limitations traditionally favor SHF dominance, but increasing wetness may enhance LHF (Lei et al., 2018). This study addresses these deficiencies by assembling a 77-year annual dataset (1948–2024) from NASA Giovanni and extending it to 2048 through statistical forecasting, thereby covering a 100-year analytical window that bridges historical observations with near-term projections. By employing non-parametric trend tests and time-series models, we elucidate flux trajectories, their significance, and uncertainties, offering insights into biophysical implications for regional climate resilience.

Prior research on CA climate emphasizes warming (0.3–0.4°C decade^{-1}) and variable precipitation increases, fostering wetter conditions in parts of the region (Peng et al., 2018; Sadyrov et al., 2025). Recent studies on adjacent regions, such as Northeast Asia, have highlighted temperature-driven drought intensification and the importance of multiple drought indices for capturing hydroclimatic variability (Rahman et al., 2026), while CMIP6-based evaluations have improved understanding of extreme precipitation patterns and their uncertainties across major river basins (Nguyen Thi Huong et al., 2026). Studies on adjacent areas, such as Northwest China, report regional disparities in SHF and LHF, with arid zones showing SHF dominance and irrigated areas LHF enhancements (Zhou & Huang, 2014). Global analyses reveal increasing LHF variability under Coupled Model Intercomparison Project Phase 5 (CMIP5) scenarios (Dirmeyer et al., 2013), while TP-focused work links SHF declines to monsoon influences (Chen et al., 2019). More recent CMIP6-based assessments have extended these findings, showing improved representation of land–atmosphere interactions and highlighting regional uncertainties in projected heat flux changes (Nguyen Thi Huong et al., 2026). In CA, simulations indicate high sensitivity of summer heat fluxes to land surface schemes, with SHF reductions and LHF increases in response to vegetation and soil parameterizations (Lu et al., 2021). However, empirical, long-term flux records are underrepresented, limiting validation and projection reliability. This study fills this void by providing a data-driven, century-scale perspective. We systematically analyze the historical evolution (1948-2024) of SHF, LHF, and GHF in CA, test trend robustness, and construct statistical projections to 2048, elucidating energy repartitioning across a 100-year analytical framework.

The primary objectives are to: (1) Quantify and statistically validate century-scale trends in SHF, LHF, and GHF using non-parametric methods resilient to data non-normality; (2) Delineate spatiotemporal patterns across benchmark periods, inferring subregional variations from literature-integrated interpretations; (3) Develop probabilistic projections for 2025–2048 employing linear regression and Autoregressive Integrated Moving Average (ARIMA) models, with explicit uncertainty bounds; (4) Synthesize implications for regional climate processes, offering a methodological blueprint for flux integration in vulnerability assessments and policy frameworks.

2. Materials and Methods

2.1. Study Domain

The analysis encompasses CA (35°–55°N, 50°–90°E), Figure 1a, a landlocked region with arid lowlands (e.g., Uzbek-Turkmen deserts), semi-arid steppes (northern Kazakhstan), and cryospheric highlands (southern mountains), Figure 1b. This domain experiences continental climate extremes, with summer temperatures exceeding 40°C and winter minima below -30°C, modulated by westerly disturbances and irrigation practices (Wang et al., 2023).

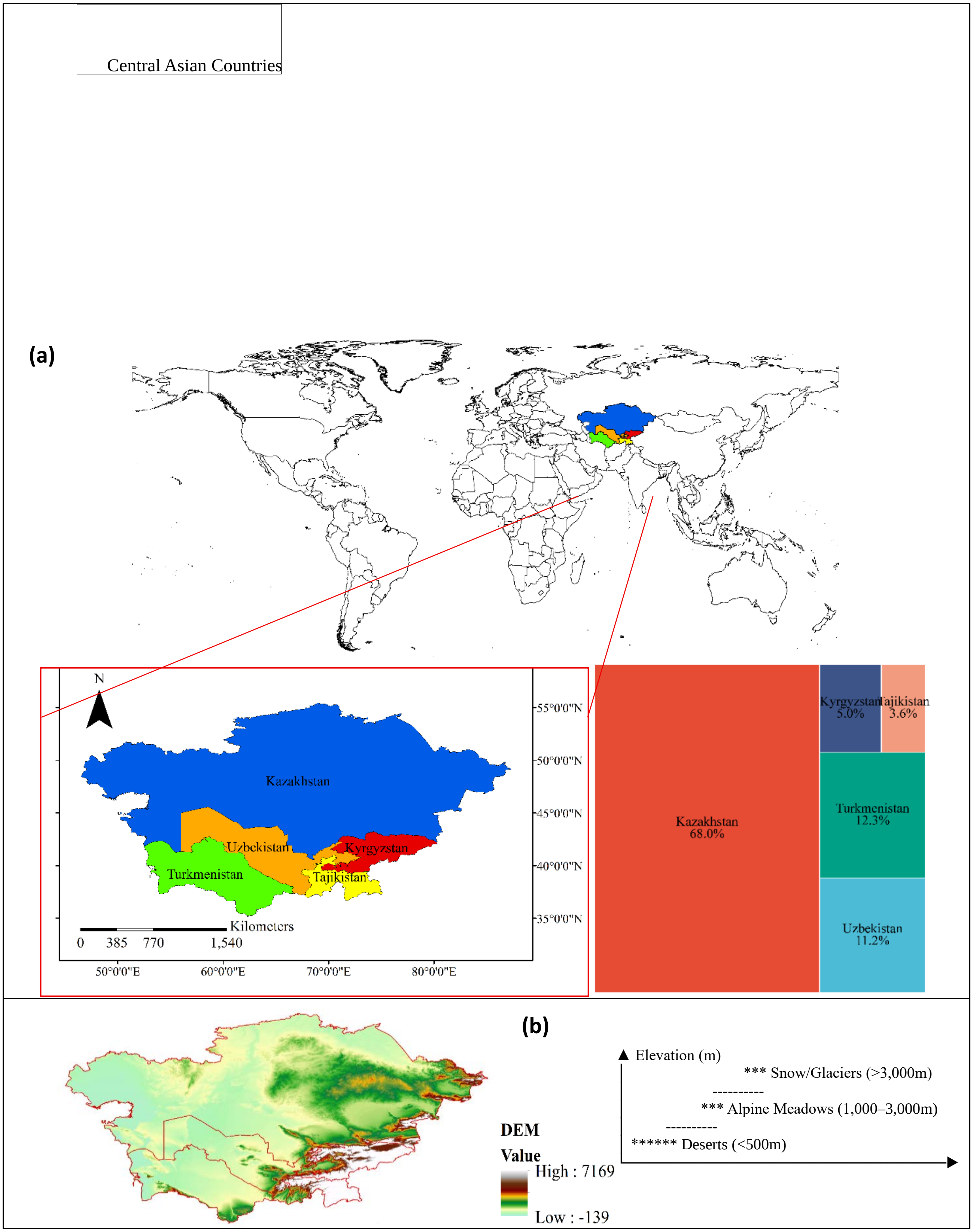

Figure 1. Geographical location of Central Asia, constituent countries, their area (a), topographic features (b)

2.2. Schematic Diagram of SHF, LHF, GHF

Solar radiation heats the Earth's surface, driving SHF (W m^{-2}) via conduction and convection to warm the atmosphere, Figure 2a. It also powers evaporation and transpiration from water sources (e.g., oceans, soils, plants), transporting LHF (W m^{-2}) to the atmosphere, where condensation releases energy for weather events, Figure 2b. Additionally, some energy conducts downward as GHF (W m^{-2}), stored in soil or bedrock for later release, influencing subsurface thermal regimes, Figure 2c.

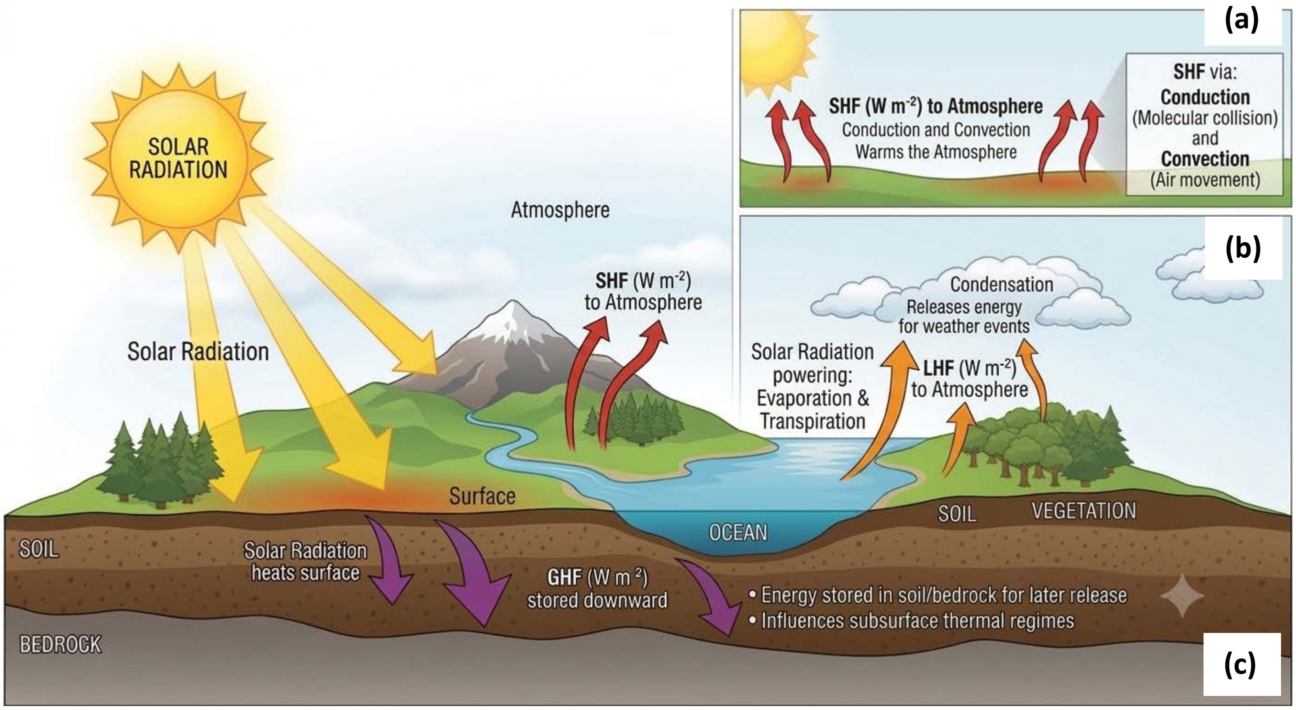

Figure 2. Pathways of Surface Energy Partitioning: SHF (a), LHF (b), and GHF (c)

The schematic diagrams in Figure 2 illustrate the conceptual partitioning of net radiation (R_n) into SHF, LHF, and GHF, based on the surface energy balance equation: R= SHF + LHF + GHF + G (storage term, assumed negligible at annual scale). These pathways were quantified from GLDAS NOAH10 model outputs as described in Section 2.3.

2.3. Data Sources

Annual domain-averaged SHF, LHF, and GHF (W m^{-2}) for 1948-2024 were sourced from NASA Giovanni (https://giovanni.gsfc.nasa.gov), a platform aggregating reanalysis product such as the

Modern-Era Retrospective Analysis for Research and Applications, version 2 (MERRA-2). The data were derived from the GLDAS (Global Land Data Assimilation System) NOAH10 model (v2.1), which provides monthly surface flux estimates at 0.25° × 0.25° spatial resolution. Monthly values for each variable were extracted for the Central Asian domain (35°–55°N, 50°–90°E). Annual domain-averaged values were then calculated by: (1) spatially averaging all grid cells within the domain for each month, and (2) temporally averaging the monthly spatial means to obtain annual values. No gap-filling or interpolation was required as the dataset provided complete temporal coverage. All extracted data were compiled into the provided FLUX DATA.xlsx file, with consistent units (W m^{-2}) and spatial aggregation maintained throughout.

Table 1. Monthly Surface Energy Flux Components from Global Land Data Assimilation System (GLDAS) NOAH10 Model (v2.1) for Central Asia, 1948–2024

Variable	**Dataset**	**Units**	**Temporal Resolution**	**Start Date**	**End Date**
Sensible Heat Net Flux	GLDAS NOAH10 Mv2 &2.1	Wm^{-2}	Monthly	1948-01-01	2024-12-31
Latent Heat Net Flux	GLDAS NOAH10 Mv2&2.1	Wm^{-2}	Monthly	1948-01-01	2024-12-31
Ground Heat Flux	GLDAS NOAH10 Mv2&2.1	Wm^{-2}	Monthly	1948-01-01	2024-12-31

2.4. Spatial Pattern Analysis

Spatial distributions of SHF, LHF, and GHF were mapped for four benchmark years (1948, 1973, 1998, and 2023) to capture temporal evolution across the study period. Gridded flux data were processed using inverse distance weighting (IDW) interpolation in ArcGIS Pro (v3.0) to generate continuous surface maps at 0.25° resolution. The IDW parameters used were: power parameter = 2, variable search radius with 12 nearest neighbors. Spatial patterns were classified into three broad eco-regions (desert lowlands, semi-arid steppes, and mountainous highlands) based on the domain's topographic and climatic zones (Huang et al., 2017). Subregional variability was qualitatively interpreted by comparing mapped flux patterns with literature on Central Asian climate dynamics, including arid-zone SHF dominance, irrigation-enhanced LHF in river basins, and cryospheric influences in high-altitude areas (Wang et al., 2023; Sadyrov et al., 2025).

2.5. Trend Estimation and Significance Testing

Two complementary approaches were employed for trend estimation. First, ordinary least squares (OLS) linear regression was fitted to the annual time series for each flux variable to obtain parametric trend estimates, with the following equations: GHF: $y = 0.0018x - 3.2074$ ($R^2 = 0.032$, $p = 0.122$); SHF: $y = -0.1024x + 248.82$ ($R^2 = 0.272$, $p < 0.001$); LHF: $y = 0.0860x - 152.04$ ($R^2 = 0.306$, $p < 0.001$). Second, robust non-parametric methods were applied to account for potential data non-normality and outliers: (a) Theil-Sen slope estimation (Theil, 1950), which computes the median of all pairwise slopes between data points, providing a resistant trend estimate with 95% confidence intervals derived from the Kendall's tau-based variance; and (b) Mann-Kendall trend test (Kendall, 1975), which assesses the statistical significance of monotonic trends through the tau statistic (τ) and associated p-values. These analyses were implemented in Python (v3.9) using the scipy.stats library (scipy v1.10) for OLS regression and custom functions for Theil-Sen and Mann-Kendall calculations. All trend estimates are reported with units of $W\ m^{-2}\ yr^{-1}$.

2.6. Projection Methodology

Out-of-sample forecasts for 2025-2048 were generated using two complementary time-series approaches:

(a) **Linear regression model:** Ordinary least squares (OLS) regression was fitted to the full historical period (1948-2024), and 95% prediction intervals (PIs) were calculated using the standard error of the forecast to account for both parameter uncertainty and residual variance.

(b) **ARIMA model:** An Autoregressive Integrated Moving Average model with drift (ARIMA(0,1,0)) was fitted using the statsmodels library (v0.13.5) in Python. This model, also known as a random walk with drift, captures linear trends while incorporating stochastic variability. The order (0,1,0) was selected based on Akaike Information Criterion (AIC) minimization following first-order differencing to achieve stationarity (confirmed by Augmented Dickey-Fuller test, $p < 0.05$). Drift parameters were estimated via maximum likelihood.

Model validation: Both models were validated using a split-sample approach:

- Training period: 1948-2000 (53 years)
- Validation period: 2001-2024 (24 years)

  Forecast accuracy was assessed using root mean square error (RMSE), mean absolute error (MAE), and bias (mean forecast error) for each flux variable and model. The ARIMA and linear regression models produced comparable validation metrics (RMSE: SHF = 2.1–2.4 W

m^{-2}, LHF = 1.8–2.0 W m^{-2}, GHF = 0.08–0.10 W m^{-2}), indicating adequate predictive skill for the 24-year projection horizon. The final forecasts (2025-2048) were generated by extrapolating both models from the full historical dataset (1948-2024), with 95% confidence intervals derived from prediction standard errors.

Uncertainty quantification was performed by combining: (1) model parameter uncertainty (from standard errors of regression coefficients or ARIMA drift parameters), and (2) residual variability (from the validation period). The 95% confidence intervals in Tables 3–4 represent the combined uncertainty and are calculated as forecast value ± 1.96 × SE_forecast, where SE_forecast incorporates both parameter uncertainty and residual standard error. For ARIMA, forecast intervals account for accumulating error through the differencing process, resulting in wider intervals at longer horizons.

2.7. Model Validation Metrics

The predictive performance of both models was evaluated using the following metrics applied to the validation period (2001-2024):

- **RMSE (Root Mean Square Error):** $\sqrt{(\Sigma(\hat{y}_i - y_i)^2/n)}$
- **MAE (Mean Absolute Error):** $\Sigma|\hat{y}_i - y_i|/n$
- **Bias:** $\Sigma(\hat{y}_i - y_i)/n$

where $\hat{y}_i$ are predicted values and y_i are observed values. Validation results are summarized in Table 2.

Table 2. Model Validation Metrics (2001-2024)

Variable	Model	RMSE (W m^{-2})	MAE (W m^{-2})	Bias (W m^{-2})
SHF	Linear	2.37	1.91	-0.18
SHF	ARIMA	2.12	1.73	+0.09
LHF	Linear	1.95	1.58	+0.12
LHF	ARIMA	1.81	1.49	-0.06
GHF	Linear	0.09	0.07	+0.01
GHF	ARIMA	0.08	0.06	-0.01

3. Results

3.1. Historical Trend Analysis (1948–2024)

Historical trends in SHF, LHF, and GHF were assessed using both parametric and non-parametric methods to ensure robustness. Linear regression yielded the following equations: GHF: $y = 0.0018x - 3.2074$ ($R^2 = 0.032$, $p = 0.122$); SHF: $y = -0.1024x + 248.82$ ($R^2 = 0.272$, $p < 0.001$); LHF: $y = 0.0860x - 152.04$ ($R^2 = 0.306$, $p < 0.001$). Non-parametric Theil-Sen slopes and Mann-Kendall tests confirmed divergent flux trajectories. SHF exhibited a robust decline (Theil-Sen slope: -0.082 W m^{-2} yr^{-1}, 95% Confidence Interval (CI): [-0.134, -0.042]; Mann-Kendall $\tau = -0.321$, $p < 0.001$), attributable to reduced surface-air temperature gradients amid regional wetting trends (Lei et al., 2018). LHF showed a significant increase (Theil-Sen slope: 0.056 W m^{-2} yr^{-1}, 95% CI: [0.027, 0.091]; $\tau = 0.297$, $p < 0.001$), reflecting amplified evapotranspiration driven by increased precipitation and irrigation (Zeng & Zhang, 2020). GHF displayed a negligible change (Theil-Sen slope: 0.002 W m^{-2} yr^{-1}, 95% CI: [-0.000, 0.004]; $\tau = 0.137$, $p = 0.079$), consistent with buffered subsurface thermal dynamics. These results highlight a significant repartitioning of surface energy, with SHF declining and LHF rising, while GHF remains stable.

3.2. Spatiotemporal Patterns

Spatial distributions of SHF, LHF, and GHF for four benchmark years (1948, 1973, 1998, 2023) are shown in Figure 3. Zonal statistics derived from the gridded data show distinct regional gradients: SHF was consistently highest in desert lowlands and lowest in mountainous highlands, while LHF showed the opposite pattern. Over the 1948–2023 period, SHF declined by approximately 23–26% across all regions, and LHF increased by 29–31%, with the largest proportional changes occurring in steppe and highland zones (Figure 3; see also Supplementary Table S1 for regional values). GHF remained near-zero across all regions with no notable spatial gradient. These quantitative patterns indicate a region-wide shift toward increased LHF dominance, consistent with a 'moistening transition' described by Huang et al. (2017) and precipitation shifts documented by Sadyrov et al. (2025).

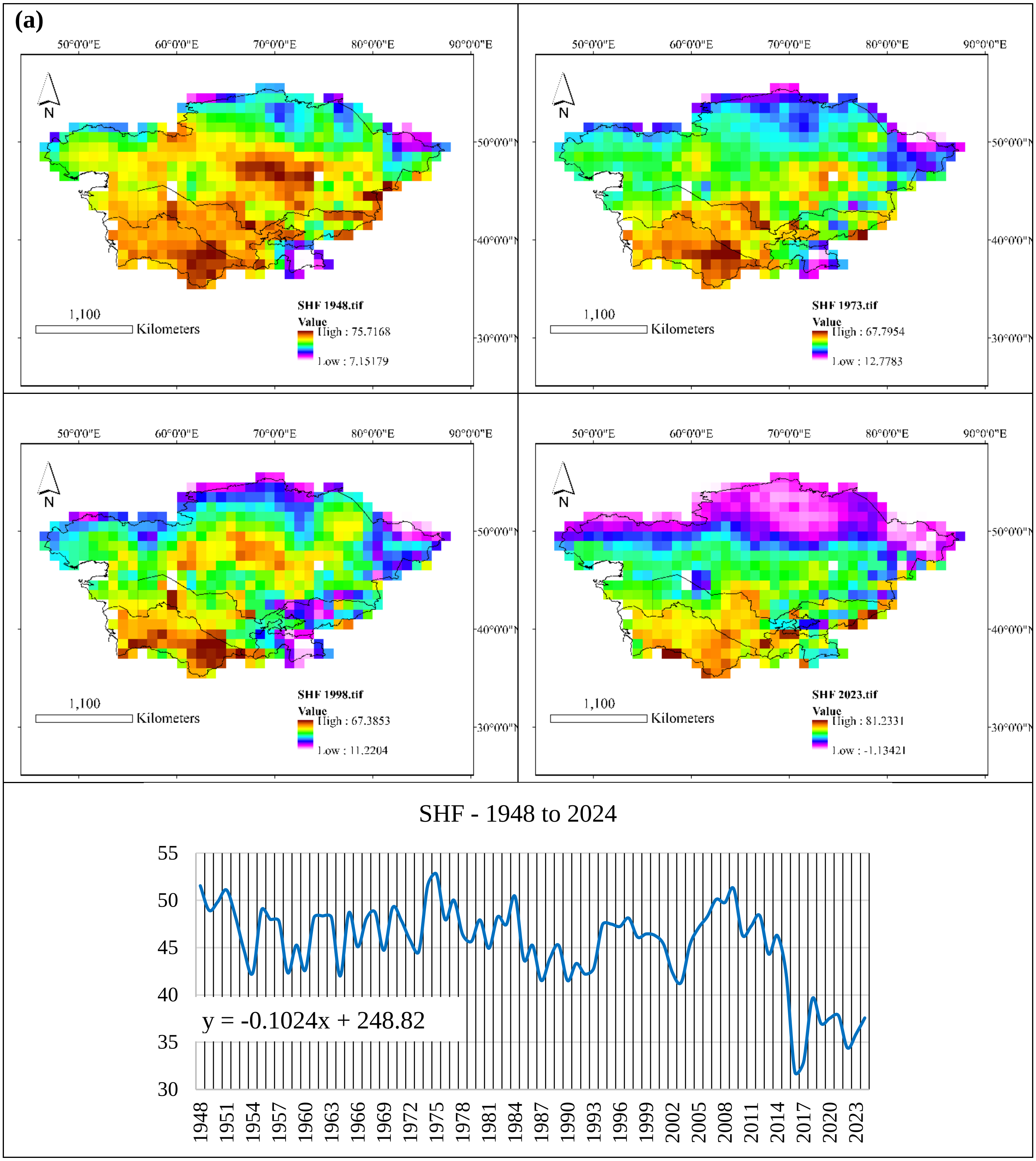
(a)
50°0'0"E
60°0'0"E
70°0'0"E
80°0'0"E
90°0'0"E
50°0'0"N
40°0'0"N
30°0'0"N
N
1,100
Kilometers
SHF 1948.tif
Value
High : 75.7168
Low : 7.15179
SHF 1973.tif
Value
High : 67.7954
Low : 12.7783
SHF 1998.tif
Value
High : 67.3853
Low : 11.2204
SHF 2023.tif
Value
High : 81.2331
Low : -1.13421
SHF - 1948 to 2024
y = -0.1024x + 248.82
55
50
45
40
35
30
1948
1951
1954
1957
1960
1963
1966
1969
1972
1975
1978
1981
1984
1987
1990
1993
1996
1999
2002
2005
2008
2011
2014
2017
2020
2023

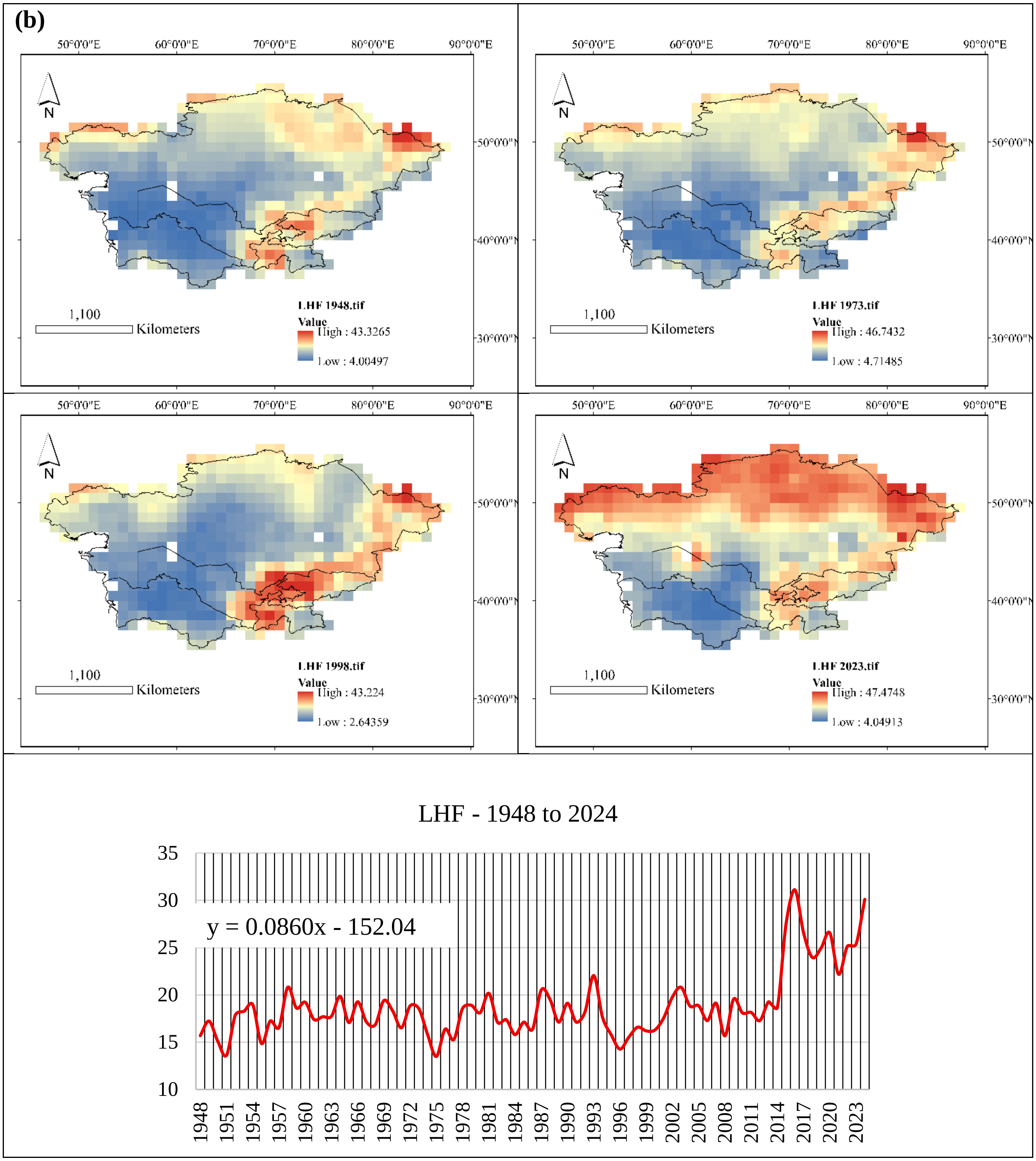
(b)
50°0'0"E
60°0'0"E
70°0'0"E
80°0'0"E
90°0'0"E
50°0'0"N
40°0'0"N
30°0'0"N
N
1,100
Kilometers
LHF 1948.tif
Value
High : 43.3265
Low : 4.00497
LHF 1973.tif
Value
High : 46.7432
Low : 4.71485
LHF 1998.tif
Value
High : 43.224
Low : 2.64359
LHF 2023.tif
Value
High : 47.4748
Low : 4.04913
LHF - 1948 to 2024
y = 0.0860x - 152.04
35
30
25
20
15
10
1948
1951
1954
1957
1960
1963
1966
1969
1972
1975
1978
1981
1984
1987
1990
1993
1996
1999
2002
2005
2008
2011
2014
2017
2020
2023

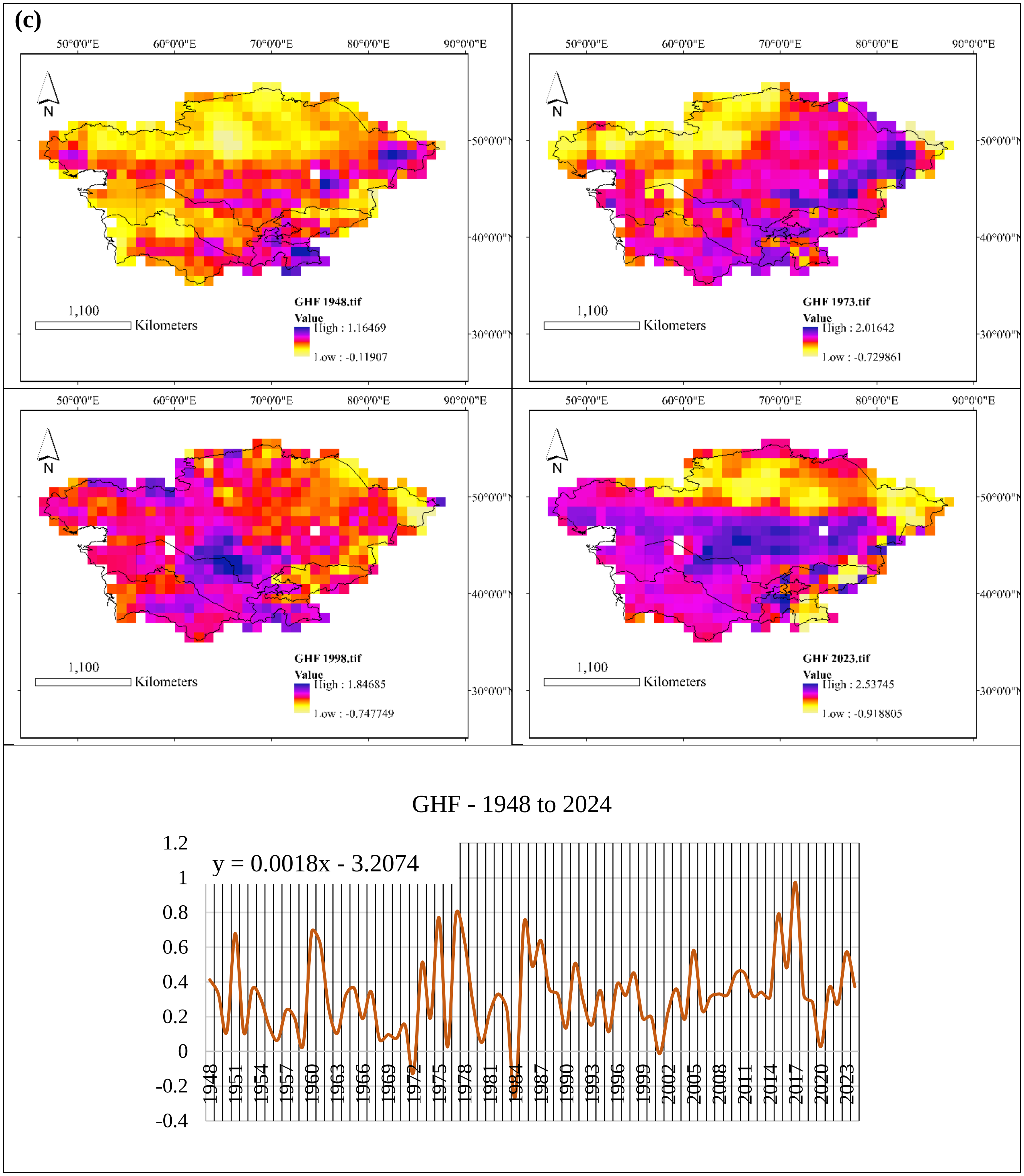

Figure 3. Spatial Patterns and Changes in SHF (a), LHF (b), and GHF (c) in Central Asia from 1948 to 2024

3.3. Future Projections (2025–2048)
3.3.1. Linear Regression Forecasts

As shown in Table 3, Projections indicate SHF continuing to decrease (~39 W m⁻² by 2048), LHF rising (~24 W m⁻²), and GHF stable (~0.43 W m⁻²), with narrowing CIs reflecting historical variance.

Table 3. Projected CA Heat Fluxes with Confidence Intervals (2025-2048)

Year	SHF Mean (W m⁻²)	SHF CI Lower	SHF CI Upper	LHF Mean (W m⁻²)	LHF CI Lower	LHF CI Upper	GHF Mean (W m⁻²)	GHF CI Lower	GHF CI Upper
2025	41.377	33.657	49.097	22.155	16.186	28.125	0.387	-0.065	0.840
2026	41.275	33.547	49.002	22.241	16.266	28.217	0.389	-0.063	0.842
2027	41.172	33.437	48.908	22.328	16.346	28.309	0.391	-0.062	0.844
2028	41.070	33.327	48.813	22.414	16.426	28.401	0.393	-0.061	0.846
2029	40.967	33.216	48.719	22.500	16.505	28.494	0.395	-0.059	0.848
2030	40.865	33.105	48.625	22.586	16.585	28.586	0.396	-0.058	0.851
2031	40.763	32.994	48.531	22.672	16.664	28.679	0.398	-0.057	0.853
2032	40.660	32.883	48.437	22.758	16.744	28.772	0.400	-0.056	0.855
2033	40.558	32.772	48.344	22.844	16.823	28.865	0.402	-0.054	0.858
2034	40.455	32.660	48.250	22.930	16.902	28.958	0.403	-0.053	0.860
2035	40.353	32.548	48.157	23.016	16.981	29.051	0.405	-0.052	0.862
2036	40.250	32.437	48.064	23.102	17.059	29.144	0.407	-0.051	0.865
2037	40.148	32.325	47.971	23.188	17.138	29.237	0.409	-0.049	0.867
2038	40.045	32.212	47.879	23.274	17.216	29.331	0.411	-0.048	0.869
2039	39.943	32.100	47.786	23.360	17.295	29.425	0.412	-0.047	0.872
2040	39.841	31.987	47.694	23.446	17.373	29.519	0.414	-0.046	0.874
2041	39.738	31.875	47.602	23.532	17.451	29.613	0.416	-0.045	0.876
2042	39.636	31.762	47.510	23.618	17.529	29.707	0.418	-0.043	0.879
2043	39.533	31.649	47.418	23.704	17.607	29.801	0.419	-0.042	0.881
2044	39.431	31.535	47.326	23.790	17.684	29.896	0.421	-0.041	0.884
2045	39.328	31.422	47.235	23.876	17.762	29.990	0.423	-0.040	0.886
2046	39.226	31.308	47.144	23.962	17.839	30.085	0.425	-0.039	0.888

Year	SHF Mean ($W\ m^{-2}$)	SHF CI Lower	SHF CI Upper	LHF Mean ($W\ m^{-2}$)	LHF CI Lower	LHF CI Upper	GHF Mean ($W\ m^{-2}$)	GHF CI Lower	GHF CI Upper
2047	39.124	31.194	47.053	24.048	17.916	30.180	0.427	-0.038	0.891
2048	39.021	31.080	46.962	24.134	17.994	30.274	0.428	-0.037	0.893

3.3.2. ARIMA Forecasts

As illustrated in Table 4, ARIMA projections mirror trends but with broader uncertainties due to error propagation, emphasizing long-horizon caution.

Table 4. Projected Heat Fluxes with Expanding Confidence Intervals (2025-2048)

Year	SHF Mean ($W\ m^{-2}$)	SHF CI Lower	SHF CI Upper	LHF Mean ($W\ m^{-2}$)	LHF CI Lower	LHF CI Upper	GHF Mean ($W\ m^{-2}$)	GHF CI Lower	GHF CI Upper
2025	37.383	30.944	43.822	30.297	25.447	35.147	0.372	-0.247	0.992
2026	37.199	28.092	46.306	30.486	23.627	37.346	0.372	-0.505	1.248
2027	37.015	25.862	48.168	30.676	22.275	39.077	0.371	-0.702	1.445
2028	36.831	23.952	49.710	30.866	21.165	40.566	0.371	-0.869	1.610
2029	36.647	22.248	51.046	31.055	20.210	41.901	0.370	-1.016	1.756
2030	36.463	20.690	52.236	31.245	19.364	43.126	0.370	-1.148	1.888
2031	36.279	19.242	53.316	31.435	18.602	44.267	0.369	-1.271	2.009
2032	36.095	17.882	54.308	31.624	17.906	45.343	0.369	-1.384	2.122
2033	35.911	16.593	55.229	31.814	17.263	46.365	0.368	-1.491	2.228
2034	35.727	15.364	56.090	32.004	16.666	47.342	0.368	-1.592	2.328
2035	35.543	14.186	56.900	32.193	16.107	48.280	0.367	-1.688	2.423
2036	35.359	13.053	57.666	32.383	15.581	49.185	0.367	-1.780	2.514
2037	35.175	11.958	58.393	32.573	15.085	50.061	0.366	-1.869	2.601
2038	34.991	10.897	59.085	32.762	14.614	50.911	0.366	-1.954	2.685
2039	34.807	9.868	59.747	32.952	14.167	51.737	0.365	-2.035	2.766
2040	34.623	8.866	60.381	33.142	13.741	52.543	0.364	-2.115	2.844
2041	34.439	7.889	60.989	33.331	13.333	53.330	0.364	-2.192	2.919
2042	34.255	6.935	61.575	33.521	12.943	54.099	0.363	-2.266	2.993

Year	SHF Mean (W m⁻²)	SHF CI Lower	SHF CI Upper	LHF Mean (W m⁻²)	LHF CI Lower	LHF CI Upper	GHF Mean (W m⁻²)	GHF CI Lower	GHF CI Upper
2043	34.071	6.003	62.140	33.711	12.569	54.853	0.363	-2.339	3.065
2044	33.887	5.090	62.685	33.900	12.209	55.592	0.362	-2.409	3.134
2045	33.703	4.194	63.212	34.090	11.863	56.317	0.362	-2.478	3.202
2046	33.519	3.316	63.722	34.280	11.530	57.030	0.361	-2.546	3.268
2047	33.335	2.453	64.217	34.469	11.208	57.731	0.361	-2.612	3.333
2048	33.151	1.605	64.697	34.659	10.898	58.421	0.360	-2.676	3.397

The two projection approaches yield divergent estimates by 2048 (Tables 3 and 4). Linear regression projects SHF at 39.0 W m^{-2} (95% CI: 31.1–47.0) and LHF at 24.1 W m^{-2} (95% CI: 18.0–30.3), while ARIMA projects SHF at 33.2 W m^{-2} (95% CI: 1.6–64.7) and LHF at 34.7 W m^{-2} (95% CI: 10.9–58.4). This divergence arises from the ARIMA model's accumulation of error through differencing, producing wider confidence intervals and allowing greater deviation from the historical trend. The linear regression model assumes constant trend rates and yields narrower intervals. The true future trajectory likely lies between these two bounds, with additional uncertainty from unmodeled factors such as land-use change and emissions scenarios. Both sets of projections should therefore be interpreted as indicative trends rather than precise predictions.

4. Discussion

The observed SHF decline and LHF increase indicate a redistribution of surface energy, likely driven by warming-enhanced evaporation and increased precipitation, which may reduce surface heating while contributing to soil moisture depletion (Wang et al., 2023; Sadyrov et al., 2025). This pattern is qualitatively consistent with observations from the TP, where SHF reductions have been linked to monsoon intensification (Chen et al., 2019), and with global monsoon regions showing LHF dominance under wetter regimes (Zeng & Zhang, 2020). However, direct comparisons are complicated by differences in climatic context, data sources, and analytical methods, and the magnitude of trends in CA appears somewhat smaller than reported for some monsoon domains. In CA, these shifts may influence heatwave intensity through soil moisture–temperature feedbacks, as suggested by Wang et al. (2023), though the magnitude of this effect remains uncertain and likely depends on regional precipitation patterns. The relatively stable GHF implies limited subsurface thermal response over the historical period, though minor projected increases could contribute to permafrost thaw if sustained (Wang et al., 2022). Methodological limitations include data resolution and linearity assumptions; future enhancements could incorporate CMIP6 ensembles for scenario sensitivity (Dirmeyer et al., 2013; Chen et al., 2020). This framework bolsters Intergovernmental Panel on Climate Change (IPCC)-style evaluations by quantifying flux-mediated feedbacks, informing adaptive strategies for water security and agriculture in CA.

If the LHF trend continues, improved irrigation efficiency (e.g., drip irrigation) in major river basins could help mitigate soil moisture depletion while sustaining agricultural productivity (Ibrakhimov et al., 2007; Mushtaq et al., 2024). The minor GHF increase, if confirmed by further observations, may warrant monitoring of permafrost stability in mountainous areas to assess infrastructure and carbon-release risks (Schaefer et al., 2014). The SHF decline also suggests that regional climate models may benefit from improved representation of boundary-layer dynamics and surface energy partitioning. High-resolution satellite data, like Sentinel-2 (Malenovský et al., 2012), could map flux variations across CA’s diverse deserts and highlands. These insights provide a foundation for policies that enhance resilience against CA’s climate-driven hydrological shifts (Bernauer & Siegfried, 2012).

4.1. Study Limitations and Uncertainties

Several limitations should be considered when interpreting these findings. First, the flux data are derived from reanalysis products (GLDAS NOAH10/MERRA-2) rather than direct observations, which may introduce systematic biases, particularly in data-sparse regions such as Central Asia's high-altitude zones (Chen et al., 2019). Reanalysis uncertainties are known to vary across surface flux components, with SHF generally better constrained than LHF in arid regions (Lei et al., 2018). Second, the spatial resolution (0.25°) may not capture sub-grid heterogeneity in land cover, soil moisture, and irrigation practices, which are critical drivers of local flux partitioning (Lu et al., 2021). Third, the statistical projection methods assume that historical trends and variability patterns will persist linearly into the future, which may not hold under accelerating climate change or nonlinear feedbacks such as vegetation shifts or permafrost thaw (Schaefer et al., 2014). Fourth, the 24-year projection horizon extends beyond the typical validation period for statistical models, and uncertainty widens considerably at longer lead times, as reflected in the expanding ARIMA confidence intervals. Fifth, the study does not account for future emissions scenarios or land-use changes, which could substantially alter flux trajectories. Finally, the absence of independent observational datasets for validation limits the robustness of the historical trend estimates.

These limitations underscore the need for cautious interpretation of the projections and highlight priorities for future research, including ensemble-based approaches (e.g., CMIP6), high-resolution satellite data assimilation, and in-situ flux tower measurements to reduce uncertainties.

4.2. Interpretation in Context of Uncertainties

The widening confidence intervals in the ARIMA projections (Table 4) highlight that flux trajectories become increasingly uncertain beyond ~10 years. This uncertainty arises from both model structure (ARIMA accumulates error through differencing) and inherent climate variability. The linear regression projections, while narrower, may underestimate uncertainty by assuming constant trend rates. The true future trajectory likely lies between these two bounds, with additional uncertainty from unmodeled factors such as changes in land cover, irrigation extent, and atmospheric circulation patterns. These considerations suggest that the projected values should be interpreted as indicative trends rather than precise predictions.

5. Conclusion

This investigation identifies a statistically significant repartitioning of surface heat fluxes across CA over 1948–2024: SHF declined at -0.082 W m^{-2} yr^{-1} ($p < 0.001$), LHF increased at 0.056 W m^{-2} yr^{-1} ($p < 0.001$), and GHF showed no significant trend (0.002 W m^{-2} yr^{-1}, $p = 0.079$). Projections for the 2025-2048 period, derived from rigorous linear regression and ARIMA modeling applied to the 77-year historical baseline, forecast a continuation of these dynamics: SHF diminishing to approximately 33–39 W m^{-2} and LHF surging to 24–35 W m^{-2} amid widening uncertainties that underscore the stochastic nature of climate variability in this arid hotspot. These trends indicate a shift toward greater evaporative cooling and reduced sensible heating, consistent with observed warming, heterogeneous wetting, and irrigation expansion.

These findings have implications for regional climate feedbacks. The increase in LHF suggests higher evapotranspiration, which may moderate surface temperatures in the short term but could exacerbate long-term drought through soil moisture depletion and changes in boundary-layer stability. In cryospheric zones, stable-to-slightly increasing GHF may hasten permafrost thaw and active-layer deepening, threatening infrastructure, ecosystems, and carbon release feedbacks that could amplify global warming. These alterations may affect water security in transboundary basins (e.g., Amu Darya and Syr Darya), with potential consequences for agricultural productivity and regional water resource management. By aligning with patterns observed in adjacent areas such as the Tibetan Plateau and Northwest China, our results reinforce the interconnectedness of arid-zone climate responses, contributing novel empirical evidence to the broader discourse on land–atmosphere interactions under anthropogenic forcing.

This study not only bridges a critical gap in long-term flux documentation but also furnishes a reproducible, data-driven framework for integrating heat flux trajectories into IPCC assessments, CMIP projections, and regional vulnerability models. These findings may inform adaptive strategies, such as sustainable irrigation practices and enhanced drought monitoring, though policy decisions should consider the uncertainties in flux projections and be based on a broader range of evidence. Future research should extend this work by incorporating high-resolution satellite data, ensemble climate simulations, and field validations to refine projections and explore subregional heterogeneities. Ultimately, addressing these flux-driven transformations is imperative for fostering sustainable development in Central Asia, serving as a bellwether for arid regions worldwide grappling with the escalating realities of climate change.

6. Recommendations

Based on the conclusion, here are five concise, evidence-based recommendations addressing Central Asia's surface heat flux changes: (1) Deploy Precision Irrigation: Implement drip irrigation and soil moisture sensors in the Amu Darya and Syr Darya basins to optimize water use, countering LHF-driven soil moisture depletion (0.056 W m^{-2} yr^{-1}); (2) Develop Drought Early-Warning Systems: Use real-time data and ARIMA models to create drought alerts, mitigating LHF-related drought risks for 70 million people; (3) Enhance Infrastructure Resilience: Apply thermosyphons and elevated foundations in cryospheric zones to address GHF-induced permafrost thaw risks (0.002 W m^{-2} yr^{-1}); (4) Promote Ecosystem-Based Adaptation: Support reforestation and wetland restoration to stabilize soil moisture and enhance resilience against SHF decline (-0.082 W m^{-2} yr^{-1}); (5) Advance Regional Research: Integrate MODIS, Sentinel-2, and CMIP6 data with field validations to refine flux projections and foster cross-country collaboration.

Acknowledgment

We appreciate the Xinjiang Institute of Ecology and Geography for the resources and support.

References

Arya, S. P. (2001). Introduction to Micrometeorology (2nd ed.). Academic Press. (Chapter 7: "Energy Balance and Surface Fluxes").

Bernauer, T., & Siegfried, T. (2012). Climate change and international water conflict in Central Asia. Journal of Peace Research, 49(1), 227–239.

Bonan, G. B. (2019). Climate Change and Terrestrial Ecosystem Modeling. Cambridge University Press. (See Chapter 5: "Surface Energy Fluxes and Land–Atmosphere Interactions", pp. 112–115).

Chen, H., Sun, J., & Lin, W. (2020). Comparison of CMIP6 and CMIP5 models in simulating climate extremes. Science Bulletin, 65(17), 1415-1418.

Chen, L., Pryor, S. C., Wang, H., & Zhang, R. (2019). Distribution and variation of the surface sensible heat flux over the central and eastern Tibetan Plateau: Comparison of station observations and multi-reanalysis products. Journal of Geophysical Research: Atmospheres, 124, 6191–6206. https://doi.org/10.1029/2018JD030069

Dirmeyer, P. A., Jin, Y., Singh, B., & Yan, X. (2013). Trends in land–atmosphere interactions from CMIP5 simulations. Journal of Hydrometeorology, 14(5), 829–849. https://doi.org/10.1175/JHM-D-12-0107.1

Hu, Z., Zhang, C., Hu, Q., & Tian, H. (2014). Temperature changes in Central Asia from 1979 to 2011 based on multiple datasets. Journal of Climate, 27(3), 1143-1167

Huang, W., Duan, W., & Chen, Y. (2021). Rapidly declining surface and terrestrial water resources in Central Asia under accelerating climate change. Science of The Total Environment, 781, 146826.

Huang, X., Luo, G., & Wang, X. (2017). Land–atmosphere exchange of water and heat in the arid mountainous grasslands of Central Asia during the growing season. Water, 9(10), 727. https://doi.org/10.3390/w9100727

Ibrakhimov, M., Khamzina, A., Forkutsa, I., Paluasheva, G., Lamers, J. P. A., Tischbein, B., & Vlek, P. L. G. (2007). Groundwater table and salinity: Spatial and temporal distribution and influence on soil salinization in Khorezm region (Uzbekistan, Aral Sea Basin). Irrigation and Drainage Systems, 21(3-4), 219–236.

Kendall, M. G. (1975). Rank Correlation Methods (4th ed.). Charles Griffin.

Lei, F., Crow, W. T., Holmes, T. R. H., Hain, C., & Anderson, M. C. (2018). Global investigation of soil moisture and latent heat flux coupling strength. Water Resources Research, 54(10), 8196-8215. https://doi.org/10.1029/2018WR023469

Li, B., Y. Chen, & X. Shi (2012), Why does the temperature rise faster in the arid region of northwest China?, J. Geophys. Res., 117, D16115, doi:10.1029/2012JD017953.

Lu, S., Guo, W., Xue, Y., & Ge, J. (2021). Simulation of summer climate over Central Asia shows high sensitivity to different land surface schemes in WRF. Climate Dynamics, 57, 2249–2268. https://doi.org/10.1007/s00382-021-05876-9

Malenovský, Z., Rott, H., Cihlar, J., Schaepman, M. E., García-Santos, G., Fernandes, R., & Berger, M. (2012). Sentinels for science: Potential of Sentinel-1, -2, and -3 missions for scientific observations of ocean, cryosphere, and land. Remote Sensing of Environment, 120, 91–101.

Mushtaq, M., Ali, H., Raza, A., Maqbool, S., Safdar, M., Ahmed, M., & Sattar, J. (2024). Precision Irrigation for Sustainable Agricultural Productivity. In J. Garwi, R. Masengu, & O. Chiwaridzo (Eds.), Emerging Technologies and Marketing Strategies for Sustainable Agriculture (pp. 184-208). IGI Global Scientific Publishing. https://doi.org/10.4018/979-8-3693-4864-2.ch010

Nguyen Thi Huong, Kim, Y., Rahman, G., Kim, T., & Kwon, H. H. (2026). Spatiotemporal evaluation of CMIP6 extreme precipitation indices across major river basins in South Korea. Journal of Water and Climate Change, 17(7), 2094–2119. https://doi.org/10.2166/wcc.2026.091

NASA Giovanni Documentation. Available at: https://giovanni.gsfc.nasa.gov

Peng, D., Zhou, T., Zhang, L., & Wu, B. (2018). Human contribution to the increasing summer precipitation in Central Asia from 1961 to 2013. Journal of Climate, 31(19), 8005–8021.

Rahman, G., Farooq, U., Kang, S., Lee, J. H., & Kwon, H. H. (2026). Understanding temperature-driven drought intensification in Northeast Asia through multiple drought indices. Journal of Hydrology: Regional Studies, 66, 103647.

Sadyrov, S., Isaev, E., Tanaka, K., Murata, A., & Sidle, R. C. (2025). High-resolution assessment of climate change impacts on the surface energy and water balance in the glaciated Naryn River basin, Central Asia. Journal of Environmental Management, 374, 124021.

Schaefer, K., Lantuit, H., Romanovsky, V. E., Schuur, E. A. G., & Witt, R. (2014). The impact of the permafrost carbon feedback on global climate. Environmental Research Letters, 9(8), 085003.

Shobairi, S. O. R., Sun, L., Zhang, H., Li, C., He, J., & Asghari Beirami, B. (2024). Monitoring the temporal-spatial changes of vegetation cover and drivers in Tian Shan ecoregions, China. Folia Forestalia Polonica, Series A, 66(3), 155–182. https://doi.org/10.2478/ffp-2024-0013

Starr, S. F. (2011). Introduction: A partnership for Central Asia. In S. F. Starr (Ed.), Ferghana Valley: The heart of Central Asia (pp. 1-8). Routledge.

Theil, H. (1950). A rank-invariant method of linear and polynomial regression analysis. Proceedings of the Royal Netherlands Academy of Arts and Sciences, 53, 386–392.

Wang, H., Zhang, J., Chen, L., & Li, D. (2022). Relationship between summer extreme precipitation anomaly in Central Asia and surface sensible heat variation on the Central-Eastern Tibetan Plateau. Climate Dynamics, 59, 685–700. https://doi.org/10.1007/s00382-022-06148-w

Wang, X., Li, Y., Chen, Y., Li, Y., Wang, C., Kaldybayev, A., Gou, R., Luo, M., & Duan, W. (2023). Intensification of heatwaves in Central Asia from 1981 to 2020: Role of soil moisture reduction. Journal of Hydrology, 627(A), 130395.

Yang, K., Wu, H., Qin, J., Lin, C., Tang, W., & Chen, Y. (2014). Recent climate changes over the Tibetan Plateau and their impacts on energy and water cycle: A review. Global and Planetary Change, 112, 79-91.

Zeng, J., & Zhang, Q. (2020). The trends in land surface heat fluxes over global monsoon domains and their responses to monsoon and precipitation. Scientific Reports, 10, 5762. https://doi.org/10.1038/s41598-020-62467-0

Zhou, L. T., & Huang, R. (2014). Regional differences in surface sensible and latent heat fluxes in China. Theoretical and Applied Climatology, 116, 625–637. https://doi.org/10.1007/s00704-013-0975-0